

# Advancing interpretation of incoherent scattering in ice penetrating radar data used for ice core site selection

Ellen Mutter<sup>1</sup> and Nicholas Holschuh<sup>2</sup>

<sup>1</sup>Department of Earth and Atmospheric Sciences, Cornell University, Ithaca, NY, 14853, USA

<sup>2</sup>Department of Geology, Amherst College, Amherst, MA 01002, USA

*Correspondence to:* Nicholas Holschuh (nholschuh@amherst.edu)

**Abstract.** Below the coherent layering in ice penetrating radar data collected in Antarctica and Greenland, incoherent scattering is common. This scattering is signal, not noise, and has the potential to inform our understanding of the structure and dynamics of the bottom 20% of glaciers and ice sheets. Here, we present a comparison between radar imagery and ice core properties for sixteen ice core sites across Antarctica and Greenland, to identify possible sources for incoherent scattering and evaluate its use in ice core site selection. We find that incoherent scattering is commonly coincident with either gradual changes in crystal orientation fabric or rapidly fluctuating fabrics in deep ice, where strain is localized by strength differences associated with ice grain size. Macro-scale deformation and layer folding at scales below the range-resolution of radar does not seem to result in incoherent scattering or induce an echo free zone, as has been previously hypothesized. Where incoherent scattering is laterally homogeneous in intensity, layering is typically undisturbed in nearby ice cores. But where incoherent scattering is laterally heterogeneous in intensity and the trace of intensity maxima does not appear conformal with subglacial topography, we find multi-meter-scale folding and associated discontinuities in nearby ice core records. Future, higher-resolution sampling of fabric in ice cores would allow for more quantitative interpretation of incoherent scattering and its amplitude, but we show that the qualitative nature of incoherent scattering has the potential to inform us about the continuity of climate records at prospective ice core sites and should be considered when evaluating the nature and quality of basal ice.

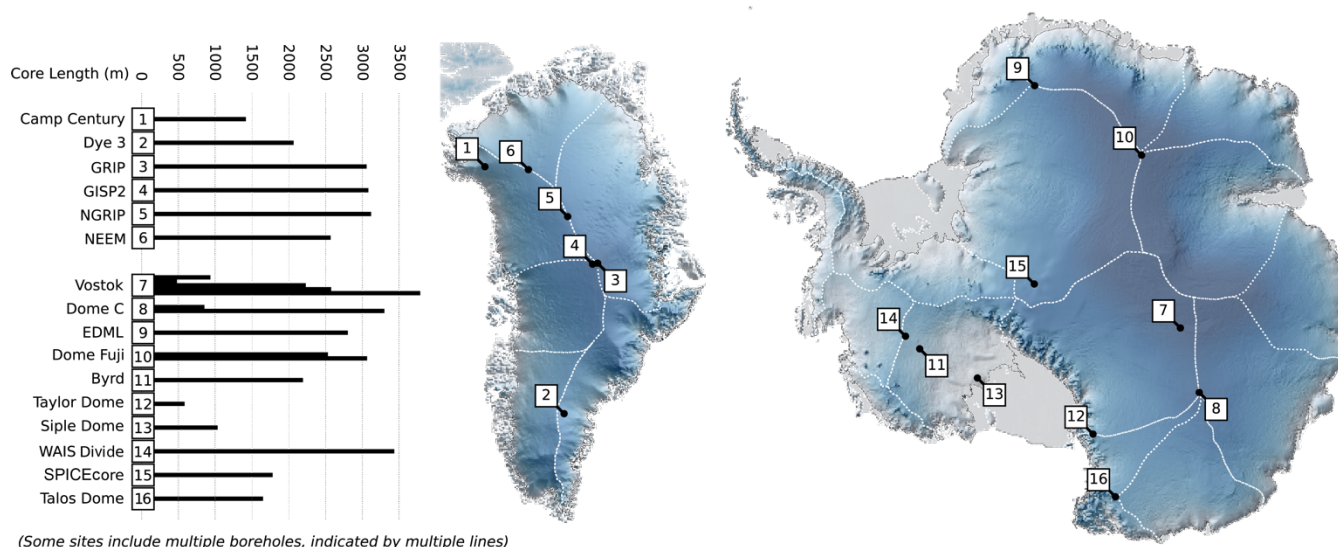
## 1. Introduction

Existing ice cores provide our best record of past atmospheric chemistry. And while they capture global climate changes over the Holocene and Late Pleistocene well (Wolff et al., 2010), future ice coring initiatives hope to build on that record, both extending it further back in time (Jouzel and Masson-Delmotte, 2010) and measuring regional climate change (Mulvaney et al., 2021) during specific climate periods (Fudge et al., 2023). These projects require the identification and collection of very specific ice, and so they typically start with extensive geophysical surveying for “site selection” preceding drilling. Ice penetrating radar data have served as the primary tool for this work, using layering in radar imagery to infer spatially variable accumulation and ice flow, and through that, identifying ideal ice core sites (Schroeder et al., 2020). But site selection has relied primarily on the strong, coherent signal that spans the shallow portions of most radar imagery. Here we focus on



31 improving interpretation of other signals in radar data, with a particular focus on what incoherent scattering (described in  
32 section 2) can tell us about ice near the ice sheet base.

33 All radio-wave scattering originates from electrical contrasts. To better understand the nature and sources of scattering in  
34 existing ice penetrating radar data, several previous studies have compared radar imagery to observations of ice chemistry and  
35 physical properties measured in ice cores (e.g., Eisen et al., 2003, 2007; Mojtabavi et al., 2022). But that work has been focused  
36 on the coherent, isochronal layering, and comparatively little has been done to understand the deeper signals, which are  
37 becoming better sampled with modern, high power / low noise systems. This deep ice has also become increasingly  
38 scientifically important, as it is at the center of the search for an ice core record that spans the Mid-Pleistocene transition (Lilien  
39 et al., 2021). Using data from 16 ice cores (fig. 1), we work to better understand the physical properties that produce deep,  
40 incoherent scattering, and evaluate the extent to which it may be diagnostic of layer disturbances or other disqualifying  
41 characteristics when pursuing future ice cores.



42  
43 **Figure 1: Locations of major ice coring initiatives in Greenland and Antarctica used in this study. On maps of Antarctica and**  
44 **Greenland, ice divides are marked in white.**

## 45 2. Background: Scattering and the Radar Imaging Problem

46 Radar systems actively transmit energy into the subsurface. Time-of-flight measurements for back-scattered energy (together  
47 with a known speed of light in ice) can be used to infer the position of subsurface scatterers and reconstruct the geometry of  
48 glacier systems (Dowdeswell and Evans, 2004). In the near sub-surface, contrasts in the dielectric permittivity that scatter



49 energy are controlled primarily by variations in density, while most deeper englacial reflectors arise from either conductivity  
50 contrasts due to variations in the concentration of free ions deposited with the snow at the surface (Stillman et al., 2013) or  
51 transitions in the ice crystal fabric, typically localized by changes in grain size also arising from impurity deposition (Fujita et  
52 al., 1999). Fabric induced scattering is a product of the dielectric anisotropy of individual ice crystals, with transitions in c-  
53 axis fabric leading to an (up to) 1% contrast in the polarization-dependent bulk permittivity. Incoherent scattering may come  
54 from both chemical and physical of sources; we work to provide some of the first constraints on its origins here.

55

56 Glaciologists primarily use radar data for ice core site selection in two ways. The first approach is focused on the geometry of  
57 coherent, isochronous layering within the ice sheet. These layers originate as flat-lying snow at the ice sheet surface and are  
58 transformed by flow during burial; thus, their geometry can be used to diagnose spatial variations in accumulation (Karlsson  
59 et al., 2020), glacier sliding (Leysinger Vieli et al., 2007), and basal melt (Fahnestock et al., 2001). The second approach is  
60 focused on the nature of subsurface scattering (its coherence, distribution, and amplitude), which can be used to infer the  
61 modern electrical (and, more generally, material) characteristics of the ice sheet and its substrate (Schroeder et al., 2020).

62

63 Subsurface targets can be divided into two main categories: specular interfaces and rough (or diffuse) scatterers (Schroeder et  
64 al., 2015). Specular interfaces, like mirrors, scatter energy in one dominant direction, a function of the direction-of-arrival for  
65 the incoming light and the orientation of the interface. Diffuse scatterers redistribute incident energy at a variety of angles.  
66 This leads to significant differences in the coherence of the scattering between specular and diffuse targets (defined here as the  
67 consistency in phase and amplitude of the backscattered energy with slight changes in the position of the radar system).  
68 Incoherent scattering typically occurs at rough interfaces or when there are multiple diffuse scattering targets in the subsurface.  
69 It has been observed as a product of rare glacier conditions, for example, where there is significant temperate ice and associated  
70 englacial water (Hamran et al., 1996) or where debris has been entrained near the base of glaciers (Winter et al., 2019). But it  
71 must also be generated by more common glaciological phenomena, as it is present within several hundred meters of the ice  
72 sheet base across large parts of Antarctica and Greenland.

73

74 Consider the example radar image in figure 2.a. Each pixel represents either backscattered energy or electrical or thermal noise  
75 in the radar electronics. The position of the radar system varies across the columns in the image, and the delay-time after the  
76 transmitted pulse (associated with the range to possible targets) varies across the rows in the image. In regions dominated by  
77 planar, specular interfaces (as in the upper half of fig. 2.a), each pixel typically represents backscattered energy from only a  
78 single subsurface target. This is because, even though there are many scattering targets at the range associated with that pixel  
79 (as shown in fig. 2.b), only that interface tangential to the range shell (such that the interface is normal to the propagating  
80 wave) returns energy to the system. But in regions where there are diffuse scatterers, each pixel in a radar image represents the  
81 interference of scattering from multiple targets (fig. 2.b.ii/iii). With slight changes in the position of the system, the dominant  
82 source of scattering at a given range can change, resulting in little consistency in phase or amplitude from pixel to pixel. This



83 is extremely common for energy arriving below the ice bottom reflector, with a long tail of incoherent scattering appearing at  
84 greater range (fig. 2.a.iii). Less well described is incoherent scattering from within the ice column (fig. 2.a.ii) which is the  
85 focus of our research here.

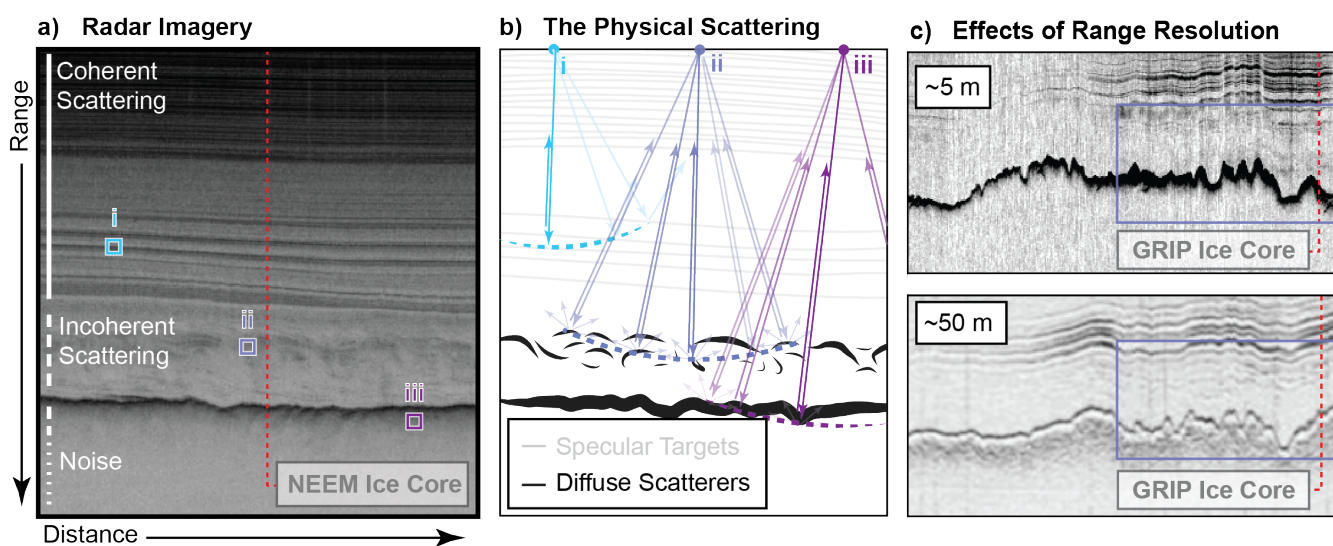
86

87 When considering the nature of scattering in radar imagery, it is important to remember that the images themselves are  
88 ultimately a product of three things:

- 89 1. The geometry and physical/electrical characteristics of the glacier subsurface.
- 90 2. The system used to collect the data (including the characteristics of the transmitted wave, antennas, and  
91 transmit/receive electronics).
- 92 3. The filtering, focusing, and additional image processing algorithms applied after collection.

93 The nature of radar targets depends on both the scale of electromagnetic heterogeneity in the medium and the frequency content  
94 of the transmit pulse (with higher frequencies / bandwidths associated with finer range resolution). Figure 2.c demonstrates  
95 how the same targets manifest differently across different radar systems; with lower resolution systems, scattering appears  
96 more structured, like the specular and coherent layering in the shallow ice. Because some systems used for site selection do  
97 not preserve phase information, we focus here primarily on the amplitude and character of scattering, controlling for differences  
98 in system characteristics.

99



100

101 **Figure 2: Example radar image (a), the ray-paths associated with scattering targets that contribute to individual pixels in the radar**  
102 **imagery (b), and a pair of images highlighting the effect of system characteristics on the nature of deep scattering (c).**

103



104 To generate incoherent scattering, deep ice must differ from the planar, layered structure of the shallow ice column in some  
105 way. It may be that incoherent scattering occurs because chemical layering is mechanically disturbed in the deep ice and is no  
106 longer planar. Or, it may be that other processes (like dynamic recrystallization or grain rotation) acting locally (due to  
107 enhanced stress near obstacles to flow, transitions in the basal thermal state, or fluidity contrasts in the ice) introduce lateral  
108 heterogeneity in physical properties that produce incoherent scattering. Here, we compile radar data from a variety of  
109 geophysical campaigns, including ground-based and airborne surveys conducted by the Center for Remote Sensing and  
110 Integrated Systems (CREStS), the British Antarctic Survey (BAS), the University of Texas (UT), the University of Washington  
111 (UW), and the Alfred Wegener Institute (AWI) – (see Supplementary Table 1 for full system characteristics). From those data,  
112 we analyze representative, ice core adjacent radar images, and compare them to measurements of crystal orientation fabric and  
113 micro- and macro-scale structures, to test two hypotheses:

- 114 1. That transitions in ice COF are collocated with (and likely induce) incoherent scattering.
- 115 2. That small scale deformation of chemically distinct layering can induce incoherent scattering.

### 116 **3. Data and Methods: Measurements Capturing the Fine- and Large-Scale Electrical Structure of Ice Cores**

117 Folds and layer disturbances at all scales have been observed or inferred from ice core records in both Antarctica and  
118 Greenland. Some scales of folding are more easily detected – millimeter and centimeter scale folds can be measured directly  
119 within the ~8 cm diameter ice cores. Folding at the 100s of meters scale is resolvable by radar. But all scales in between must  
120 be inferred, using anomalous patterns of electrical conductivity, stable isotope or impurity concentrations, or physical and  
121 optical properties. We summarize the measurements that we use to identify deformation in deep ice below, and aim to relate  
122 radio-wave scattering phenomena to these observations.

123  
124 Physical analysis of ice cores, including macro-scale visual observations and optical imaging (i.e. line scanners) (Faria et al.,  
125 2018; Jansen et al., 2015; Svensson, 2005), and alternating current and direct current electrical conductivity measurements  
126 (Fudge et al., 2016; Wolff, 2000) provide the best direct measurement of small scale features deep in the ice column. The  
127 resolution of typical line scan images is around 0.1 mm/pixel, allowing for observations of layers and their structure ranging  
128 from millimeter-scale undulations up to folds at scale of the typical ~8 cm diameter of deep ice cores. Data from ice core line-  
129 scanning have shown wavy strata (e.g. WAIS (West Antarctic Ice Sheet) Divide, (Fitzpatrick et al., 2014)), highly inclined  
130 strata (e.g. EDML (EPICA Dronning Maud Land), (Faria et al., 2018)) and large z-folds (e.g. NEEM (North Greenland Eemian  
131 Ice Drilling), (Jansen et al., 2015)), capturing unique forms of stratigraphic disturbance and in some cases, informing the depth  
132 associated with discontinuities in the climate record.

133  
134 In addition to imaging methods that capture small scale deformation, a range of chemical methods have been employed across  
135 deep ice core sites to identify major breaks in stratigraphic continuity and large-scale folding. Some breaks in continuity have



136 been identified using chemical disagreement between ice cores. For cores in the same geographic region (e.g. GISP2  
137 (Greenland Ice Sheet Project Two), GRIP (Greenland Ice Core Project), and NorthGRIP (North Greenland Ice Core Project)),  
138 divergence in electrical conductivity, delta  $\delta^{18}\text{O}$  of ice ( $\delta^{18}\text{O}_{\text{ice}}$ ), and impurity concentrations can be used to identify the onset  
139 of a discontinuous record (Johnsen et al., 2001). When looking across hemispheres, divergence in the profiles of globally well-  
140 mixed delta  $\delta^{18}\text{O}$  of atmospheric  $\text{O}_2$  ( $\delta^{18}\text{O}_{\text{atm}}$ ) and  $\text{CH}_4$  have been used to identify climate record discontinuity (Chappellaz et  
141 al., 1997; Landais et al., 2003). In cases where there are no cores that provide high resolution comparison, sudden shifts in the  
142 nature of the chemical signal (e.g. changes in chemical variability or abrupt changes in the gas-age ice-age difference, described  
143 as either the  $\Delta\text{age}$  between the ice and gas or the depth-shift separating gas and ice of a constant age) have been used to infer  
144 climate record discontinuities (Crotti et al., 2021; Dansgaard, 1982; Jouzel et al., 2007; Petit et al., 1999; Ruth et al., 2007).  
145 Chemical methods have also been used to reconstruct chronologies in heavily disturbed stratigraphy (Landais et al., 2003;  
146 NEEM Community Members, 2013; Raynaud et al., 2005; Souchez et al., 2002; Verbeke et al., 2002), and from those  
147 chronologies, identify overturned folding. These methods have in some places tentatively inferred (e.g., at Vostok and GRIP)  
148 and in other places clearly identified (at NEEM) folding on scales of 10-100 m.

149  
150 In addition to measurements capturing macro-scale deformation, crystallographic analysis of glacial ice, typically performed  
151 using vertical and/or horizontal thin sections of ice cores, provides two useful pieces of information for our work.  
152 Measurements of the bulk c-axis orientation of glacial ice gives us direct constraint on how the polarization-dependent  
153 permittivity of ice might vary with depth, and therefore be a source of scattering. It also provides information about the strain  
154 history of ice, with implications for larger-scale deformation in the ice column. C-axis orientation can be measured with a  
155 range of techniques, including polarized light microscopy (Azuma et al., 1999; Weikusat et al., 2017; Wilson et al., 2003), x-  
156 ray diffraction and tomography (Miyamoto et al., 2011), sonic wave methods (Kluskiwicz et al., 2017), electron backscatter  
157 diffraction microscopy (Obbard and Baker, 2007), and open resonator methods (Saruya et al., 2024).

158  
159 Historically, data from thin sections have provided the most robust evidence of differential strain at small scales, capturing  
160 fabric changes within a single 10 cm vertical thin section (e.g. NEEM, (Montagnat et al., 2014)). But the logistics of thin  
161 section sampling limits their ability to capture some scales of vertical and horizontal variability in fabric. The distance between  
162 adjacent, discrete thin-section samples can be anywhere from 20 to 100+ m (e.g. EDML (Weikusat et al., 2013), Siple Dome  
163 (Gow and Meese, 2007), NorthGRIP (Wang et al., 2002), GRIP (Thorsteinsson et al., 1997)). New approaches to c-axis  
164 characterization may change what is possible in future studies of fabric derived scattering, as open resonator methods using  
165 0.5 m thick sections of ice have been used to measure the clustering of crystal c-axes every 20 mm along the Dome Fuji core  
166 (Saruya et al., 2022, 2024). But for most available data, we are limited in our ability to quantitatively predict scattering from  
167 existing fabric measurements, as the magnitude of backscatter depends on the depth-rate-of-change of fabric. Instead, we focus  
168 primarily on qualitative comparison of fabric changes with radar images.



### 169 **3. Results: Investigating the Sources of Incoherent Scattering**

170 We present measured fabric and structural data together with radar imagery across 9 well sampled cores in Figure 3, and  
171 evaluate the depth-agreement of scattering, known fabric transitions, and small- and large-scale deformation below. A full  
172 description of the ice core data used can be found in Supplementary Table 2.

#### 173 **3.1 Crystal fabric transitions as a source of incoherent scattering**

174 Given the enhanced stresses and therefore higher strain-rates near the base of ice sheets, one might expect monotonic but  
175 intensifying fabric development with depth. And at the majority of ice core drill sites, c-axis fabrics transition from a quasi-  
176 isotropic c-axis distribution at the top of the ice column to strong single maxima lower in the column (e.g. Camp Century,  
177 Dye-3, GISP2, NEEM, Dome C, Talos Dome, GRIP), a product of the typical simple shear near the base of a glacier. Ice cores  
178 drilled at flank sites or otherwise away from ice divides can also experience uniaxial horizontal extension, and thus c-axis  
179 fabrics transition from quasi-isotropic to girdle-type fabric and then to a single maximum (e.g. NorthGRIP, Vostok, EDML).  
180 But variability in the impurity content (which can vary with changes in climate) can intensify fabric development and localize  
181 fabric transitions, with fabric strengthening typically coincident with higher impurity content (seen at Byrd (Faria et al., 2014),  
182 Camp Century (Faria et al., 2014), Talos Dome (Montagnat et al., 2012), Dome C (Durand et al., 2009), NEEM (Montagnat  
183 et al., 2014), GISP2 (Gow et al., 1997), and Dye-3 (Langway et al., 1988)).

184  
185 Abrupt fabric transitions occurs at most ice core sites in Greenland (e.g. Camp Century, Dye-3, GISP2, and NEEM), where a  
186 significant change in impurity deposition at the Holocene-Wisconsin climate transition is co-located with an abrupt  
187 strengthening or transition to a vertical-maximum fabric (Faria et al., 2014). In some places, we see an isolated but abrupt  
188 transition in fabric that has co-located scattering in the radar image. At NEEM, a transition from a weak vertical girdle to  
189 strong single maximum fabric occurs at 1419 m and is coincident with a diffuse reflector in the radargram (fig. S1). Similar,  
190 reflectors appear at isolated fabric transitions in Antarctica as well. At Siple Dome, the c-axis fabric transitions from a vertical  
191 girdle to a single maxima at 700 m, with a corresponding diffuse reflector in the radar data. At EDML, the c-axis fabric  
192 transition from a vertical girdle to a strong single maxima between 2025 and 2045 m has been identified as the origin of the  
193 reflector at 2035 m (Eisen et al., 2007). These reflectors appear less specular (with trailing energy after the initial arrival) than  
194 other isochronous layering within the radar imagery.

195  
196 Where we see well sampled gradual transitions in fabric (spanning 50-100 m of the ice column) we observe a diffuse band of  
197 incoherent scattering. At Dome C, the strong single maximum fabric at 2800 m gradually transitions to a broad single maximum  
198 fabric at 2857 m and returns to a strong single maxima fabric at 2900 m (Durand et al., 2009). This fabric transition is roughly  
199 coincident with the transition from thin coherent isochronal strata to a single diffuse incoherent scattering layer observed  
200 around 2825 m. Similarly, at Dome Fuji, the strong single maxima fabric at 2660 m gradually weakens before returning to a



201 strong single maxima fabric again at 2760 m (Saruya et al., 2024). Again, this appears roughly coincident with a diffuse  
202 incoherent scattering layer observed at ~2700 m in the radargram (fig. S2).

203

204 In many places, especially where time is compressed significantly at the base of the ice column, alternating fabrics have been  
205 observed. At Vostok, from 2700 to 3315 m depth, the core alternates between coarse grained ice with girdle-type fabric and  
206 fine grained ice with single-maximum fabric every ~100 m (Obbard and Baker, 2007). Within the girdle-type fabric zone  
207 between ~3220 and 3315 m, we see weakly banded incoherent scattering (3220 – 3290 m). Between ~3315 and 3450 m  
208 alternations between girdle-type and single-maximum fabric occur approximately every ~20 m (Lipenkov and Raynaud, 2015).  
209 This zone of increased fabric alternation overlaps with both the no echo zone between ~3290 and 3360 m and the upper depths  
210 of a weakly banded incoherent scattering unit (~3360 – 3490 m) in the radargram. While interpretation of the GISP2 and GRIP  
211 radargrams has significant ambiguity below 2800 m, 40 km length radar transects show laterally heterogeneous incoherent  
212 scattering in that depth range (fig. S3). At GRIP, each of the five thin sections sampled between 2800 and 2950 m depth show  
213 alternating fabrics. At GISP2, coarse-grained layers with fabrics that deviate from the strong single maximum are observed at  
214 increasing frequencies below 2800 m (Gow et al., 1997).

215

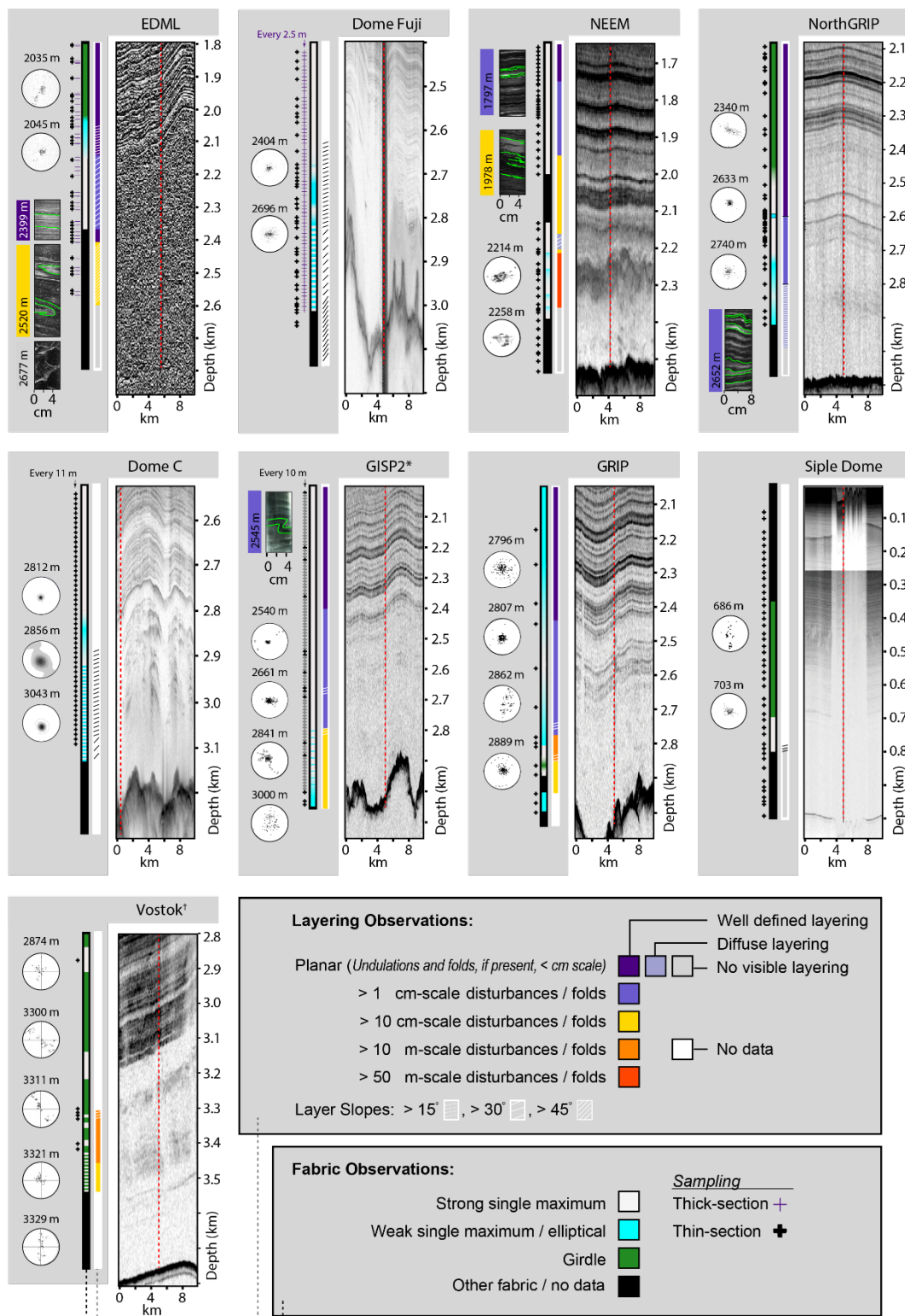
216 While challenging to constrain due to thin-section sampling frequency, the smallest scale of fabric variability has been  
217 observed or inferred at centimeter-scales, including at Vostok, Dome C, and Dome Fuji. At Vostok, fabric alternations occur  
218 at cm-scale frequency from 3450 m until the transition from meteoric to accreted ice at 3538 m (Lipenkov and Raynaud, 2015).  
219 This overlaps with an echo-free zone in the radargram. At Dome C, ice below 2800 m consists of alternating layers with high  
220 impurity content (consistently presenting strong single maxima fabric) and layers with low impurity content (with an associated  
221 broad single maximum fabric). After the gradual transition into and out of a broad single maximum fabric at 2850 m, fabric  
222 transitions below 2920 m become more local. High frequency sampling of fabric (every 0.5 m) between 2933 and 2955 m  
223 revealed fabric alternations between each sample (Durand et al., 2009). Unlike at Vostok where the onset of rapid fabric  
224 transitions coincides with the start of the echo free zone, the onset of rapid fabric transitions at Dome C is associated with thick  
225 and sometimes discontinuous bands of incoherent scattering (2900 – 3050 m) in the radargram. At Dome Fuji, cm-scale  
226 fluctuations from the single maximum fabric, observed by increases in the standard deviation of  $\Delta\epsilon$  (the difference in the  
227 relative permittivity,  $\epsilon$ , between vertical and horizontal planes), begin around 2400 m and intensify through the base of the ice  
228 column (Saruya et al., 2024). The increase in fabric fluctuations between 2400 and 2650 m has no obvious effect on the  
229 coherent continuous layering observed in the radargram. However, the Dome Fuji radargram transitions to a zone of laterally  
230 homogenous incoherent scattering at 2900 m. Notably, the precise depth of that transition is difficult to constrain in the radar  
231 image, due to the combination of increasing layer inclinations (Dome Fuji Ice Core Project Members, 2017) and strong  
232 scattering from borehole fluid in the ice core cavity (fig. S2).

233





234 The most complex scattering pattern we see is at NEEM, starting at ~2200 m. We see strong incoherent scattering that is highly  
235 laterally variable. In this section of the ice core, the same oxygen isotope sequence (and its associated fabric gradient, from  
236 multi-clustered-fabric to single maxima fabric) is repeated, with abrupt fabric transitions at the boundaries between sequences.  
237 This is attributed to overturned folds at the base of the ice column, in part, facilitated by rheologic differences in the ice that  
238 also produce the abrupt fabric transitions. Here, both fabric and larger-scale deformation likely play a significant role in the  
239 nature of the scattering, introducing lateral heterogeneity in material properties (for ice at a given depth) that doesn't exist at  
240 other ice core sites.





242 **Figure 3: Radargrams capturing deep ice at ice core drill sites where we have comprehensive fabric and deformation data. This**  
243 **includes line-scan data: EDML (Faria et al., 2018), Dome Fuji (Takata et al., 2004), NEEM (Kipfstuhl, 2009), NorthGRIP (Svensson,**  
244 **2005), GRIP (Alley et al., 1997); fabric observations: EDML (Eisen et al., 2007; Faria et al., 2018; Weikusat et al., 2013), Dome Fuji**  
245 **(Saruya et al., 2022, 2024), NEEM (Eichler, 2013; Montagnat et al., 2014), NorthGRIP (Wang et al., 2002), Dome C (Durand et al.,**  
246 **2009), GISP2 (Gow et al., 1997), GRIP (Thorsteinsson et al., 1997), Siple Dome (Gow and Meese, 2007), Vostok (Obbard and Baker,**  
247 **2007); and layering observations: EDML (Faria et al., 2010, 2018), Dome Fuji (Dome Fuji Ice Core Project Members, 2017), NEEM**  
248 **(Jansen et al., 2015), NorthGRIP (Svensson, 2005), Dome C (Durand et al., 2009), GISP2 (Alley et al., 1995, 1997; Faria et al., 2014;**  
249 **Gow et al., 1997), GRIP (Alley et al., 1995; Dahl-Jensen et al., 1997; Johnsen et al., 1995; Landais et al., 2003), Siple Dome (Gow and**  
250 **Meese, 2007), Vostok (Lipenkov and Raynaud, 2015; Raynaud et al., 2005; Souchez et al., 2002). \*At GISP2, only some of the sampled**  
251 **thin sections have published data (indicated by the black + symbols), and †at Vostok, the original sampling rate is unpublished, with**  
252 **only a few thin sections and general observations available in the literature.**

### 253 **3.2 Folding as a source of incoherent scattering**

254 Millimeter-scale disturbances are likely present in most deep glacial ice, given their ubiquity in physical observations of ice  
255 cores. But there is little evidence that deformation at that scale impacts the radiostratigraphy directly. In the South Pole Ice  
256 Core (SPICEcore), inclined and pinched cloudy bands are observed starting at 1000 m and continue at intervals through the  
257 end of the core (Fegyveresi and Alley, 2018) without any noticeable impact on radar scattering. Crystal striping at GISP2 is  
258 observed starting at 2200 m, coincident with the onset of small scale undulations in linescan images (Alley et al., 1997) but  
259 similar to SPICEcore, there is no associated change in the nature of radar layering. Millimeter-scale z-folds at GRIP first appear  
260 at 2438 m and at 2437 m at GISP2 (Alley et al., 1997), which does coincide with a drop in power of coherent scattering layers.  
261 But there is a commensurate drop in the ice conductivity variability associated with changes in dust deposition, which better  
262 explains that change. Thus, we rule out millimeter-scale folding as a significant contributor to the radar signal observed at  
263 these locations.

264  
265 Stratigraphic disturbances at the centimeter-scale are apparent in all cores with available data. In previous work, this scale of  
266 deformation has been invoked as a mechanism for the “echo free zone”, with the idea that folding effectively homogenizes  
267 dielectric contrasts at the scale of the resolution of the radar (Winter et al., 2017). At EDML and WAIS Divide, the onset of  
268 cm-scale disturbance does appear to be collocated with the apparent echo free zone. In both radar images, however, there is a  
269 gradual diminution of returned power with depth. It is possible that measured disturbances do reduce the intensity of back-  
270 scatter without eliminating it entirely. But there is laterally-continuous layering (with strong back-scatter intensities) in regions  
271 of cm-scale disturbances at NorthGRIP, NEEM, and GRIP, and in regions with disturbances at the scale of 10 cm at NEEM.  
272 Radar data at NEEM show no change in scattering behavior associated with deformation at this scale. This seems to imply that  
273 these radar systems (with range-resolutions of 2.8 m to 5 m (Table S1)) are insensitive to deformation at this scale.

274



275 But deeper in the NEEM core, where chemical analyses reveal six zones of disturbed ice including two large 50 and 100 m  
276 thick folded layers of inverted early glacial ice (NEEM Community Members, 2013), high amplitude but laterally variable  
277 incoherent scattering can be seen in the radar imagery. Deformation at this scale, thought to be in part due to rheological  
278 differences between the glacial and interglacial ice (NEEM Community Members, 2013), is coincident with a loss of coherent  
279 banding in the line scan imagery and an increase in the lateral heterogeneity of intensity in incoherent backscatter. Above 3460  
280 m depth at Vostok, folding is also inferred at the meter scale and larger (Lipenkov and Raynaud, 2015). Similarly, there is  
281 incoherent scattering in the image at these depths, although the amplitude of the backscatter is weaker, and lateral heterogeneity  
282 less pronounced. Finally, at GRIP, tentative chronological reconstructions of disturbed ice below 2750 m show significant  
283 disruption and folding on the scale of 10s of meters between 2780 to 2850 m. And while near the ice core, this depth-range  
284 corresponds with a unit of weak incoherent scattering, at the 10s of kilometers scale, there is significant variability in the  
285 amplitude (fig. S3).

#### 286 **4. Discussion: Using Incoherent Scattering in Ice Core Site Selection**

287 There is compelling evidence that incoherent scattering can arise from fabric transitions in the deep ice, and the quality of that  
288 scattering could be diagnostic of large-scale deformation that is co-located with the smaller-scale fabric development. If true,  
289 then incoherent scattering might be used to improve ice core site selection. We test that theory at 16 ice core sites, by first  
290 subdividing core-adjacent radar imagery into five types of signal (fig. 4):

- 291
- 292 1. Laterally continuous coherent scattering (that is, clear isochronal layering)
- 293 2. Diffuse but banded scattering
- 294 3. Laterally homogenous incoherent scattering
- 295 4. Laterally heterogeneous incoherent scattering
- 296 5. No signal (or rather, signal levels at or below the noise floor of the system).

297

298 We then compare these scattering types to known breaks in the continuity of the associated ice cores (see Appendix A for the  
299 observational basis for each labelled break).

300

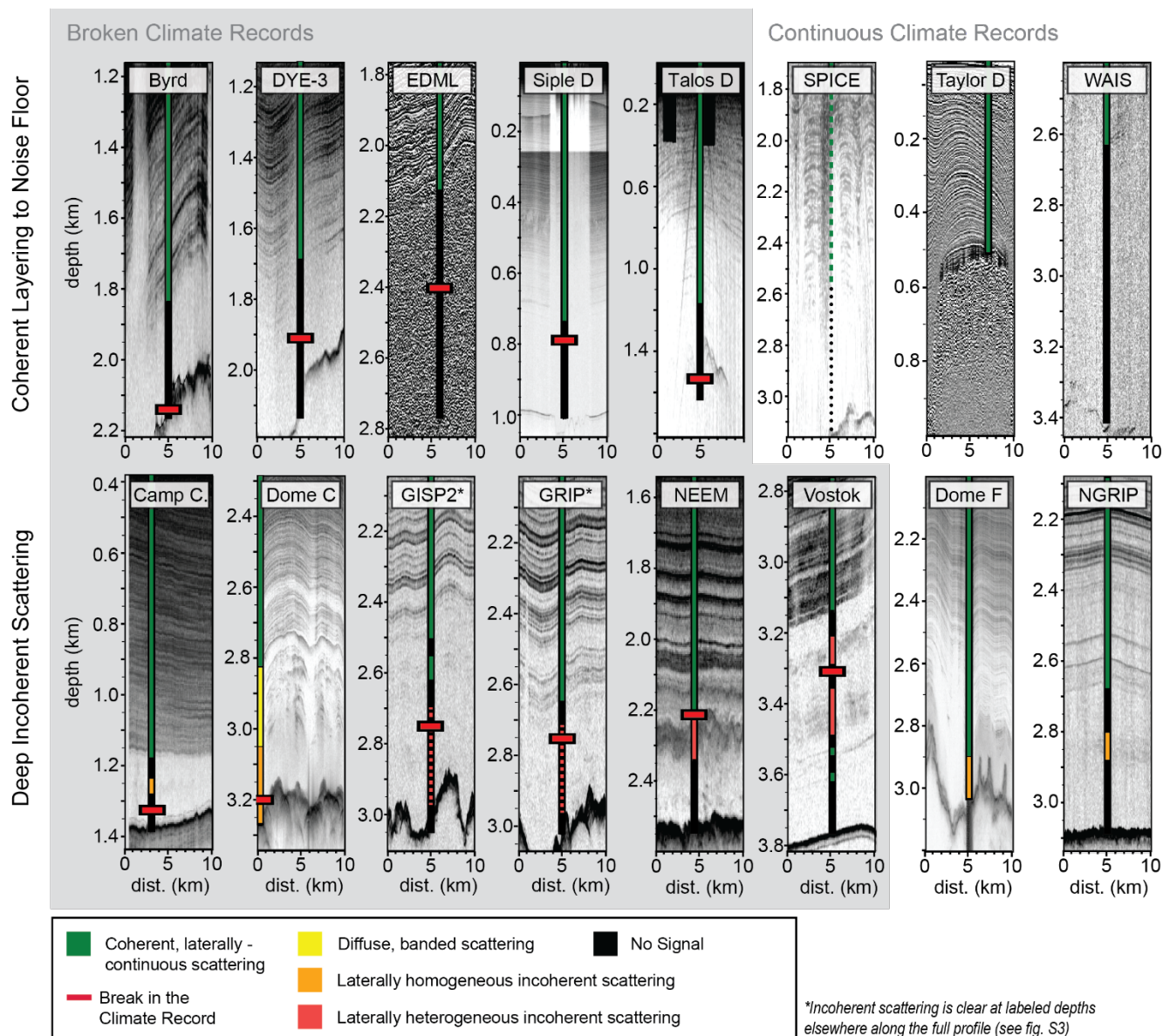
301 Across these core sites, continuous coherent scattering is almost exclusively found above known breaks in the climate record.  
302 This type of scattering appears below the break in a climate record in only one ice core, and that is Vostok, where the interface  
303 between accreted and meteoric ice and a layer of mineral inclusions from the lake bed (Turkeev et al., 2021), define two clear  
304 reflection horizons. As a result, in typical glaciological environments, continuous coherent scattering is a robust indicator of  
305 ice core continuity. At the studied core sites, where diffuse but banded scattering sits immediately below laterally continuous



306 layering, there are no associated breaks in measured climate records. This supports the idea that banded but incoherent  
307 scattering is not an indication of disturbed basal ice.

308  
309 Where we see laterally homogenous incoherent scattering, as in Camp Century, Dome C, Dome Fuji, and NorthGRIP, it occurs  
310 within sections of ice with a continuous climate record. This likely indicates fabric transitions that are themselves defined  
311 weakly by depositional impurities, and thus, the shape of the scattering band is roughly parallel to the isochronous layering.  
312 At Vostok, we see laterally incoherent scattering that is heterogeneous in its intensity but is otherwise layering conformal,  
313 directly above and ~100 - 200 m below the broken climate record. These two bands of incoherent scattering are qualitatively  
314 indistinguishable, and demonstrate the challenge of interpreting the quality of the climate record within bed conformal laterally  
315 heterogeneous incoherent scattering regions. But where we see laterally heterogeneous incoherent scattering that is layering  
316 non-conformal (as in GISP2, GRIP, and NEEM) it occurs below breaks in the continuity of the observed climate record. In  
317 those places, it is possible that the same ice rheology contrast that facilitated a fabric transition together with a complex basal  
318 stress regime enabled multi-meter scale deformation, inducing lateral variability in the backscatter intensity, and indicating  
319 significant risk of a disturbed climate record.

320



321

322

323

324

**Figure 4: Radar images collected proximal to ice core sites. For each core site, the core location, depth, and breaks in the climate record are labeled. In addition, we categorize the scattering observed in the radar imagery as a function of depth at each core site. Metadata for the radargrams is presented in Supplementary Table 1.**



## 325 5. Conclusions

326 Based on comparison between ice core data and radar imagery at ice core sites, we show that diffuse and incoherent scattering  
327 is often colocated with transitions in the crystal orientation fabric of the ice. Transitions in fabric are a product of the local  
328 stress regime, but they are localized by differences in grain size. High concentrations of impurities tend to reduce local grain-  
329 size and enhance deformation rates, so where climatically driven variations in impurities change the strength of the ice, one  
330 might also expect more abrupt contrasts in fabric that back-scatter radio waves. In this way, fabric controlled scattering may  
331 be roughly isochronous, although we show that fabric interfaces do not manifest as abrupt, specular reflectors the way  
332 chemically induced layering does in radar imagery.

333  
334 In the deep ice, where stresses are high, time is compressed, and global changes in impurity deposition are expressed over  
335 narrower depth ranges, we might expect fabric induced scattering is common. The nature of the fabric transition, and the spatial  
336 heterogeneity in the transition, define whether or not the scattering will appear as coherent layering, a diffuse scattering  
337 horizon, laterally homogenous incoherent scattering, or laterally heterogeneous incoherent scattering. In addition, ice fluidity  
338 contrasts at fabric boundaries facilitate small- and large-scale folding. At small scales (below ~1 m), folding seems to have  
339 little impact on existing radar data. But large-scale folding, where present, results in complex scattering targets in the  
340 subsurface, and induces significant lateral heterogeneity in the incoherent scattering intensity and complex scattering horizons.  
341 Where this is observed at existing ice core sites, it seems indicative of discontinuities in the ice core climate record.

342  
343 A final consideration when thinking about fabric induced incoherent scattering is the relationship between permittivity  
344 contrasts (as experienced by the propagating radio-wave) and radio-wave polarization. For fabric intensification (for example,  
345 a weak single maximum to a strong single maximum fabric) there will be a change in permittivity for all radar polarizations,  
346 and scattering will likely appear isotropic. For fabric transitions (for example, from a girdle to a single maximum fabric) it is  
347 possible for some polarizations to exhibit scattering and others to have low backscatter or apparent echo free zones. This  
348 anisotropic character merits further study at places like Siple Dome, EDML, and Vostok, where girdles are seen in the deep  
349 ice.

350  
351 As is true for discussions of the “echo free zone”, we show that conversations about the “basal layer” observed in Greenland  
352 and Antarctica must start from the understanding that deep scattering (or its absence) depends on system characteristics and  
353 physical properties of the ice. Both echo free zones and deep incoherent scattering could arise from multiple mechanisms. But,  
354 as with coherent layering, incoherent scattering is signal, not noise, and more work should be done to better interpret this often  
355 overlooked component of radar imagery.



356 **6. Author Contribution**

357 EM synthesized data from the literature on physical and chemical properties of ice cores and identified radar data from CReSIS,  
358 BAS, UT, UW, and AWI. All authors contributed to study design, radargram interpretation, figure creation, and writing of  
359 manuscript.

360 **7. Competing Interests**

361 The authors declare that they have no conflict of interest.

362 **8. Acknowledgements**

363 This work was funded through the Center for Oldest Ice Exploration (NSF-2019719). It also represents an aggregation of a  
364 tremendous amount of work from previous scholars studying ice cores, and we would like to thank those communities and  
365 encourage suggestions from those scholars for new ways to connect ice penetrating radar to measurable ice core quantities.

366





## 367 **Appendix A. Known Layer Disturbances and Ice Core Continuity Problems**

368 Of the cores studied, 5 show only minor signs of layer disturbances, and contain a continuous climate record through the full  
369 depth range of the ice core. Those are Dome Fuji, NorthGRIP, SPICEcore, Taylor Dome, and WAIS Divide. Of the other 11  
370 cores, 6 have well identified breaks in their climate record, and 4 are likely discontinuous (although the exact stratigraphic  
371 break is not well identified), and 1 has conflicting observations of discontinuity. Here, we describe the observational basis for  
372 claims of a broken climate record.

### 373 **A.1 Cores with Clear Evidence of Stratigraphic Discontinuities**

374 *(Alphabetically: EDML, GRIP, GISP2, NEEM, Talos Dome, Vostok)*

375  
376 **EPICA (European Project for Ice Coring in Antarctica) Dronning Maud Land, EDML (Length: 2774 m | Break: 2417**  
377 **m | Percentage Disturbed: 12.9%):** The chronology called EDML1 has been established for the top 2417 m of the EDML  
378 ice core. The top 2366 m of the core is matched to the EDC3 chronology using volcanic signatures (dielectric profiling, SO<sub>4</sub>  
379 concentrations, and electrolyte conductivity measurements) (Ruth et al., 2007). Three tie points between the EDC3 chronology  
380 and EDML core are matched between 2366 and 2415 m using insoluble dust concentrations,  $\delta^{18}\text{O}$ , and  $\delta\text{D}$ , however these  
381 matches are considered uncertain with estimated errors up to several thousand years (Ruth et al., 2007). Macrostructure analysis  
382 of linescan images between 2400 and 2500 m shows evidence of large-scale folding (Faria et al., 2010).

383  
384 **Greenland Ice Core Project, GRIP (Length: 3029 m | Break: ~2750 m | Percentage Disturbed: 9.2%) and Greenland**  
385 **Ice Sheet Project Two, GISP2D (Length: 3053.4 m | Break: ~2750 m | Percentage Disturbed: 9.9%):** CH<sub>4</sub> and  $\delta^{18}\text{O}_{\text{atm}}$   
386 data from both GRIP and GISP2 show evidence of stratigraphic disturbance in the bottom 10% the ice cores. Above 2750 m  
387 CH<sub>4</sub> and  $\delta^{18}\text{O}_{\text{atm}}$  values vary synchronously between GRIP and GISP2, but below 2750 m, the chemical profiles diverge,  
388 showing large and significant fluctuations which are not present in the undisturbed ice from the Vostok 3G core (Chappellaz  
389 et al., 1997).

390  
391 **North Greenland Eemian Ice Drilling, NEEM (Length: 2540 m | Break: 2209.6 m | Percentage Disturbed: 13%):** At  
392 NEEM, an abrupt discontinuity in the  $\delta^{18}\text{O}_{\text{ice}}$  at 2209.6 m marks the end of synchronization with the NorthGRIP GICC05  
393 extended timescale. Additional discontinuities in the  $\delta^{18}\text{O}_{\text{ice}}$  subdivide the bottom 13% of the core into six zones of disturbed  
394 stratigraphy. These correspond with similar shifts in other atmospheric gas measurements (CH<sub>4</sub>,  $\delta^{18}\text{O}_{\text{atm}}$ , N<sub>2</sub>O,  $\delta^{15}\text{N}$  of N<sub>2</sub>).  
395 Within the upper five zones, the layering is thought to be unbroken (based on continuous records of N<sub>2</sub>O,  $\delta^{15}\text{N}$  of N<sub>2</sub>, dust, or  
396 electrical properties), with timescales for each of the upper five zones reconstructed by synchronizing NEEM  $\delta^{18}\text{O}_{\text{atm}}$  and CH<sub>4</sub>  
397 profiles with NorthGRIP and EDML records. The timescales for these zones include inverted, mirrored, and folded ice up to  
398 100 m thick (NEEM Community Members, 2013).



399

400 **TALos Dome Ice CorE, TALDICE (Length: 1620 m | Break: 1548 m | Percentage Disturbed: 4.4%):** At Talos Dome,  
401 Crotti et al. identify a break in stratigraphic continuity at 1548 m using analysis of  $\delta^{18}\text{O}_{\text{atm}}$ ,  $\delta\text{D}$ , and  $81\text{Kr}$  dating, described  
402 below (Crotti et al., 2021). TALDICE  $\delta^{18}\text{O}_{\text{atm}}$  and  $\delta\text{D}$  measurements were matched to the EDC  $\delta^{18}\text{O}_{\text{atm}}$  and  $\delta\text{D}$  record through  
403 visual synchronization through 1548 m depth. Below 1548 m, the amplitude of  $\delta^{18}\text{O}_{\text{atm}}$  fluctuations is damped, making  
404 synchronization with the EDC record uncertain. Similarly, below 1548 m, the TALDICE  $\delta\text{D}$  signal becomes asynchronous  
405 with the EDC record.  $81\text{Kr}$  dating of three samples below 1548 m depth revealed that ice from 1613 - 1618 m had comparable  
406 age to samples from 1559 - 1563 m and 1573 - 1578 m depth, indicating a disturbed age-depth relationship.

407

408 **Vostok 5G-5 (Length: 3658 m | Break: 3311 m | Percentage Disturbed: 9.5%):** The stratigraphy in the bottom 9% of the  
409 Vostok 5G core is divided between 228 m of disturbed meteoric ice, and 119 m of accreted lake ice. In the upper part of the  
410 disturbed meteoric ice, the lack of depth-shift between  $\delta\text{D}_{\text{ice}}$  and gas measurements ( $\text{CO}_2$  and  $\text{CH}_4$ ) is interpreted by Souchez  
411 et al. as evidence of folding and intermixing (Souchez et al., 2002). Observations of ash layers with depth-varying inclinations  
412 supports interpretation of large-scale folding. In the lower part of the disturbed meteoric ice, damped variation of  $\delta\text{D}_{\text{ice}}$  and  
413 trace impurity distributions ( $\text{Na}^+$ ,  $\text{Cl}^-$ , non-sea salt  $\text{Mg}^{++}$  and  $\text{Ca}^{++}$ ), physical observations of interbedded fine-grained  
414 (presumably glacial) and coarse-grained (presumably interglacial) ice, and the presence of bed material in the bottom 100 m  
415 of the disturbed meteoric ice, is interpreted as further evidence for stratigraphic deformation (Lipenkov and Raynaud, 2015;  
416 Souchez et al., 2002). At 3538 m depth, the transition between meteoric and accreted ice is apparent from the  $\delta\text{D}_{\text{ice}}/\delta^{18}\text{O}$   
417 fingerprint of freezing processes (Jouzel et al., 1999). At this depth, sudden transitions to lower total gas content, increased  
418 crystal size, low ECM values, increased  $\delta\text{D}_{\text{ice}}$ , and decreased deuterium excess, provide further evidence for the  
419 meteoric/accreted ice transition (Jouzel et al., 1999).

## 420 **A.2 Cores that Likely Contain Stratigraphic Discontinuities or Conflicting Observations of Discontinuity**

421 *(Alphabetically: Byrd, Camp Century, Dome C, Dye-3, Siple Dome)*

422

423 **Byrd Station '68, BYRD 68 (Length: 2164 m | Break: 2135-2144 m | Percentage Disturbed: ~1%):** A chronology for the  
424 upper ~99% (2144 m) of the Byrd core has been established by synchronizing Byrd, GRIP, and GISP2  $\text{CH}_4$  profiles (Blunier  
425 and Brook, 2001). Gas volume measurements from the bottom 10 m of the core (2154 - 2164 m) suddenly approach zero at  
426 4.83 m above the bed, revealing the transition between meteoric ice and accreted subglacial meltwater (Gow et al., 1979). The  
427 bottom 4.83 m of non-meteorice contain horizontal bands of basal debris including sand, clay, and pebbles as large as 8 cm  
428 in diameter (Gow et al., 1979). Grootes et al. 2001 observe that the Byrd  $\delta^{18}\text{O}$  record becomes asynchronous with Taylor Dome  
429 and Vostok record around 2135 m.

430



431 **Camp Century, CC 63-66 (Length: 1387.4 m | Break: ~1350 m | Percentage Disturbed: 2.7%):** The integrity of the Camp  
432 Century climate record is uncertain below 1310 m depth where  $\delta^{18}\text{O}$  profiles of Camp Century, GRIP, and GISP2 become  
433 asynchronous (Johnsen et al., 2001). Correlation of a smoothed Camp Century  $\delta^{18}\text{O}$  profile with benthic foraminifera record  
434 from deep sea core RC11-120 provides a tentative extension of the chronology through about 1330 m, the depth of the  
435 inflection point associated with Marine Isotope Stage (MIS) 5d (Dansgaard et al., 1985). A dramatic cold event at 1340 m is  
436 associated with a similar  $\delta^{18}\text{O}$  fluctuation in the disturbed section of the GRIP core at 2800 m (Johnsen et al., 2001). Johnsen  
437 et al. describe dramatic fluctuations in  $\delta^{18}\text{O}$  below Greenland Interstadial (GI) 23 in the GRIP, GISP2, and Camp Century  
438 cores which are not represented in the continuous  $\delta^{18}\text{O}$  signal from Vostok (Chappellaz et al., 1997).

439

440 **EPICA Dome C, EDC99 (Length: 3260 m | Potential Break: ~3200 m | Percentage Disturbed: ~1.8%):** The continuity of  
441 the upper 98% (3200 m) of the Dome C core is evidenced primarily through matching of  $\delta\text{D}_{\text{ice}}$  to the deep-sea benthic  $\delta^{18}\text{O}$   
442 record (Jouzel et al., 2007). Additional matching of enhanced  $^{10}\text{Be}$  deposition to Matuyama-Brunhes geomagnetic reversal  
443 between 3160 and 3170 m (Jouzel et al., 2007) and matching of  $\text{CO}_2$  and  $\text{CH}_4$  profiles to MIS18 and 19 between 3160 and  
444 3185 m further support the continuity of the upper 98% of the core. Below 3200 m, there is contradictory evidence about the  
445 continuity of the climate record. Measurements of  $\delta\text{D}$ , total air content, gas composition, and dust content suggest continuity  
446 to bedrock, while  $\delta^{18}\text{O}_{\text{atm}}$ , visible inclusions, length of the glacial period, and variability of chemical species distribution  
447 suggest altered stratigraphy (Tison et al., 2015).

448

449 **DYE-3, DYE3 79-81 (Length: 2037 m | Break: 1940 m | Percentage Disturbed: 4.8%):** At DYE-3, the continuity of the  
450 climate signal is lost between 1900 and 1987 m. Initially, Dansgaard et al. 1982 correlated fluctuations between the  $\delta^{18}\text{O}$   
451 measurements at DYE-3 and Camp Century through 1987 m depth. Between 1987 and 2010 m, DYE-3  $\delta^{18}\text{O}$  values are quasi-  
452 constant, and interpreted as evidence of folded layers. Later, comparison of the  $\delta^{18}\text{O}$  values between DYE-3 and GRIP led  
453 Johnsen et al., 2001 to identify GI 8 at 1900 m as the last undisturbed match point between the two records. However Johnsen  
454 et al. would still identify two match points in the deeper ice: GI 12 (~1925 m) and GI 14 (~1940 m). As such, in our analysis  
455 we have used 1940 m as the depth of the broken climate record.  $\text{CO}_2$  and  $\text{CH}_4$  measurements of the bottom 27 m of silty ice  
456 have been used to identify 4 distinct zones of highly deformed basal ice (Verbeke et al., 2002).

457

458 **Siple Dome A, SDMA (Length: 1004 m | Break: ~800 m | Percentage Disturbed: ~20%):** The integrity of the Siple Dome  
459 climate record is uncertain in the bottom 200 m of the core, however a precise onset depth for the disturbed ice is poorly  
460 constrained. A chronology for the 514 - 854 m section of the core was established by synchronizing Siple Dome, GISP2, and  
461 GRIP  $\text{CH}_4$  profiles (Brook et al., 2005). Below 854 m, the methane data becomes sparse however a possible chronology has  
462 been proposed between 854 and 920 m based on the matching of a single inflection point in the  $\delta^{18}\text{O}_{\text{atm}}$  profile of Siple Dome  
463 core at 920 m with a corresponding GISP2  $\delta^{18}\text{O}_{\text{atm}}$  inflection point (Brook et al., 2005). Macro and micro-scale physical  
464 observations by Gow and Meese suggest an interrupted climate record by 800 m depth, summarized here (Gow and Meese,



465 2007). Between 560 and 800 m, sequences of inclined layering occasionally surpassing 10 degrees as well as reversed dips are  
466 observed. Below 800 m the core is highly fractured, limiting any further observations of layer structure. Around 700 m, the c-  
467 axis fabric shifts suddenly to a single maximum corresponding to a stress regime dominated by strong horizontal shear. Around  
468 800 m, the c-axis fabric shifts back to a multi-maxima fabric.

### 469 **A.3 Cores with No Significant Break in Continuity**

470 *(Alphabetically: Dome Fuji, NorthGRIP, SPICEcore, Taylor Dome, WAIS Divide)*

471

472 **Dome Fuji, DF2 (Length: 3035.22 m):** The integrity of the Dome Fuji ice core climate record is discussed by the (Dome Fuji  
473 Ice Core Project Members, 2017) and summarized here. A chronology for the upper 3028 m of the 3035 m Dome Fuji core  
474 was established through the synchronization of  $\delta^{18}\text{O}$  records to the Dome C  $\delta\text{D}$  profile. Physical observations of inclined layers  
475 begin at 2400 m and show distinct stepwise increases in inclination:  $\sim 8^\circ$  between 2450 - 2600,  $\sim 20^\circ$  between 2600 - 2800,  
476  $\sim 40^\circ$  between 2800 - 2900,  $\sim 45^\circ$  at 2950 m, and  $\sim 50^\circ$  at bedrock. Despite the observations of inclined layers, which are  
477 attributed to spatially variable basal melt conditions, explicit observations of folded layers were not noted and the synchronicity  
478 of the  $\delta^{18}\text{O}$  and Dome C  $\delta\text{D}$  profiles are considered evidence of an intact climate record within the depths of inclined layers.

479

480 **North Greenland Ice Core Project, NorthGRIP (Length: 3090 m):** At NorthGRIP, the continuity of the 2544 – 3073 m  
481 zone of the 3090 m length core was confirmed by matching NorthGRIP  $\delta^{18}\text{O}_{\text{atm}}$  and  $\text{CH}_4$  records to EDML and EDML1  
482 chronologies (Capron et al., 2010). Depth shift analysis at 2940 m showed the expected shift between  $\delta^{15}\text{N}$  and  $\text{CH}_4$  vs  $\delta^{18}\text{O}$   
483 during Dansgaard-Oescher (DO) 24, and was used to confirm the continuity of the deepest layers (North Greenland Ice Core  
484 Project Members, 2004). Like at WAIS Divide, small scale stratigraphic disturbances are observed a few hundred meters above  
485 bedrock (Svensson, 2005), but are not considered large enough to impact the continuity of the climate record.

486

487 **South Pole Ice Core, SPICEcore, SPC14 (Length: 1500 m | Ice thickness: 2700 m):** Continuity through the end of the core  
488 is established through synchronization of  $\text{CH}_4$  fluctuations to WAIS Divide ice core (Epifanio et al., 2020). Notably,  
489 SPICEcore drilling stopped 1200 m above bedrock.

490

491 **Taylor Dome, M3C1 (Length: 554 m):** The continuity of the Taylor Dome core was established through correlation of the  
492  $\text{CH}_4$  and  $\delta^{18}\text{O}_{\text{atm}}$  profiles with corresponding GISP2 profiles as well as correlation of the  $\delta^{18}\text{O}$  profile with the Vostok  $\delta\text{D}$   
493 record (Grootes et al., 2001; Steig et al., 1998). The  $\delta^{18}\text{O}$  inflection point associated with MIS 5e ( $\sim 130\text{kyBP}$ ) is identified  
494 between 526 and 531 m depth. The identification of correlated inflection points continues confidently through 200 kyBP with  
495 a tentative chronology, limited by sample resolution, extending beyond 300 kyrBP (Grootes et al., 2001).

496



497 **WAIS (West Antarctic Ice Sheet) Divide, WDC06A (Length: 3405 m | Ice thickness: 3455 m):** The continuity of the  
498 WAIS Divide core is confirmed above 2850 m by annual layer counting, and below 2850 m via synchronization of WAIS  
499 Divide CH<sub>4</sub> measurements to the NorthGRIP  $\delta^{18}\text{O}$  record and a refined Hulu Cave speleothem  $\delta^{18}\text{O}$  record (Buizert et al.,  
500 2015). Notably, the 3405 m WAIS Divide core ends 50 m above bedrock, so continuity in the uncored 50 m basal unit is not  
501 confirmed. Mm-scale or smaller stratigraphic disturbances are observed at 3150 and 3232 m (Fitzpatrick et al., 2014) but are  
502 not considered large enough to impact the continuity of the climate record.  
503



## 504 References

- 505 Alley, R. B., Gow, A. J., Johnsen, S. J., Kipfstuhl, J., Meese, D. A., and Thorsteinsson, T.: Comparison of deep ice cores,  
506 Nature, 373, 393–394, <https://doi.org/10.1038/373393b0>, 1995.
- 507 Alley, R. B., Gow, A. J., Meese, D. A., Fitzpatrick, J. J., Waddington, E. D., and Bolzan, J. F.: Grain-scale processes, folding,  
508 and stratigraphic disturbance in the GISP2 ice core, J. Geophys. Res. Oceans, 102, 26819–26830,  
509 <https://doi.org/10.1029/96JC03836>, 1997.
- 510 Azuma, N., Wang, Y., Mori, K., Narita, H., Hondoh, T., Shoji, H., and Watanabe, O.: Textures and fabrics in the Dome F  
511 (Antarctica) ice core, Ann. Glaciol., 29, 163–168, <https://doi.org/10.3189/172756499781821148>, 1999.
- 512 Blunier, T. and Brook, E. J.: Timing of millennial-scale climate change in Antarctica and Greenland during the Last Glacial  
513 Period, Science, 291, 109–112, <https://doi.org/10.1126/science.291.5501.109>, 2001.
- 514 Brook, E. J., White, J. W. C., Schilla, A. S. M., Bender, M. L., Barnett, B., Severinghaus, J. P., Taylor, K. C., Alley, R. B.,  
515 and Steig, E. J.: Timing of millennial-scale climate change at Siple Dome, West Antarctica, during the last glacial period,  
516 Quat. Sci. Rev., 24, 1333–1343, <https://doi.org/10.1016/j.quascirev.2005.02.002>, 2005.
- 517 Buizert, C., Cuffey, K. M., Severinghaus, J. P., Baggenstos, D., Fudge, T. J., Steig, E. J., Markle, B. R., Winstrup, M., Rhodes,  
518 R. H., Brook, E. J., Sowers, T. A., Clow, G. D., Cheng, H., Edwards, R. L., Sigl, M., McConnell, J. R., and Taylor, K. C.: The  
519 WAIS Divide deep ice core WD2014 chronology – Part 1: Methane synchronization (68–31 ka BP) and the gas age–ice age  
520 difference, Clim. Past, 11, 153–173, <https://doi.org/10.5194/cp-11-153-2015>, 2015.
- 521 Capron, E., Landais, A., Lemieux-Dudon, B., Schilt, A., Masson-Delmotte, V., Buiron, D., Chappellaz, J., Dahl-Jensen, D.,  
522 Johnsen, S., Leuenberger, M., Loulergue, L., and Oerter, H.: Synchronising EDML and NorthGRIP ice cores using  $\delta^{18}\text{O}$  of  
523 atmospheric oxygen ( $\delta^{18}\text{O}_{\text{atm}}$ ) and  $\text{CH}_4$  measurements over MIS5 (80–123 kyr), Quat. Sci. Rev., 29, 222–234,  
524 <https://doi.org/10.1016/j.quascirev.2009.07.014>, 2010.
- 525 Chappellaz, J., Brook, E., Blunier, T., and Malaizé, B.:  $\text{CH}_4$  and  $\delta^{18}\text{O}$  of  $\text{O}_2$  records from Antarctic and Greenland ice: a clue  
526 for stratigraphic disturbance in the bottom part of the Greenland Ice Core Project and the Greenland Ice Sheet Project 2 ice  
527 cores, J. Geophys. Res., 102, 26547–26557, <https://doi.org/10.1029/97JC00164>, 1997.
- 528 Crotti, I., Landais, A., Stenni, B., Bazin, L., Parrenin, F., Frezzotti, M., Ritterbusch, F., Lu, Z.-T., Jiang, W., Yang, G.-M.,  
529 Fourné, E., Orsi, A., Jacob, R., Minster, B., Prié, F., Dreossi, G., and Barbante, C.: An extension of the TALDICE ice core age  
530 scale reaching back to MIS 10.1, Quat. Sci. Rev., 266, 107078, <https://doi.org/10.1016/j.quascirev.2021.107078>, 2021.
- 531 Dahl-Jensen, D., Gundestrup, N. S., Keller, K., Johnsen, S. J., Gogineni, S. P., Allen, C. T., Chuah, T. S., Miller, H., Kipfstuhl,  
532 S., and Waddington, E. D.: A search in North Greenland for a new ice-core drill site, J. Glaciol., 43, 300–306,  
533 <https://doi.org/10.3189/S0022143000003245>, 1997.
- 534 Dansgaard, W.: A New Greenland Deep Ice Core, Science, 218, 1273–1277, 1982.
- 535 Dansgaard, W., Clausen, H. B., Gundestrup, N., Johnsen, S. J., and Rygner, C.: Dating and climatic interpretation of two deep  
536 Greenland ice cores, in: Greenland Ice Core: Geophysics, Geochemistry, and the Environment, vol. 33, edited by: Langway,  
537 C. C., Oeschger, H., and Dansgaard, W., American Geophysical Union, Washington, D. C., 71–76,  
538 <https://doi.org/10.1029/GM033p0071>, 1985.
- 539 Dome Fuji Ice Core Project Members: State dependence of climatic instability over the past 720,000 years from Antarctic ice  
540 cores and climate modeling, Sci. Adv., 3, <https://doi.org/10.1126/sciadv.1600446>, 2017.



- 541 Dowdeswell, J. A. and Evans, S.: Investigations of the form and flow of ice sheets and glaciers using radio-echo sounding,  
542 *Rep. Prog. Phys.*, 67, 1821–1861, <https://doi.org/10.1088/0034-4885/67/10/R03>, 2004.
- 543 Durand, G., Svensson, A., Persson, A., Gilllet-Chaulc, F., Montagnat, M., and Dahl-Jensen, D.: Evolution of the texture along  
544 the EPICA Dome C ice core, *Physics of Ice Core Records II : Papers collected after the 2nd International Workshop on Physics  
545 of Ice Core Records*, held in Sapporo, Japan, 68, 91–105, 2009.
- 546 Eichler, J.: C-axis analysis of the NEEM ice core, Master’s Thesis, Freie Universitat, Berlin, Germany, 63 pp., 2013.
- 547 Eisen, O., Wilhelms, F., Nixdorf, U., and Miller, H.: Revealing the nature of radar reflections in ice: DEP-based FDTD forward  
548 modeling, *Geophys. Res. Lett.*, 30, <https://doi.org/10.1029/2002GL016403>, 2003.
- 549 Eisen, O., Hamann, I., Kipfstuhl, S., Steinhage, D., and Wilhelms, F.: Direct evidence for continuous radar reflector originating  
550 from changes in crystal-orientation fabric, *The Cryosphere*, 1, 1–10, <https://doi.org/10.5194/tc-1-1-2007>, 2007.
- 551 Epifanio, J. A., Brook, E. J., Buizert, C., Edwards, J. S., Sowers, T. A., Kahle, E. C., Severinghaus, J. P., Steig, E. J., Winski,  
552 D. A., Osterberg, E. C., Fudge, T. J., Aydin, M., Hood, E., Kalk, M., Kreutz, K. J., Ferris, D. G., and Kennedy, J. A.: The SP19  
553 chronology for the South Pole Ice Core – Part 2: gas chronology,  $\Delta$ age, and smoothing of atmospheric records, *Clim. Past*, 16,  
554 2431–2444, <https://doi.org/10.5194/cp-16-2431-2020>, 2020.
- 555 Fahnestock, M., Abdalati, W., Joughin, I., Brozena, J., and Gogineni, P.: High geothermal heat flow, basal melt, and the origin  
556 of rapid ice flow in Central Greenland, *Science*, 294, 2338–2342, <https://doi.org/10.1126/science.1065370>, 2001.
- 557 Faria, S. H., Freitag, J., and Kipfstuhl, S.: Polar ice structure and the integrity of ice-core paleoclimate records, *Quat. Sci. Rev.*,  
558 29, 338–351, <https://doi.org/10.1016/j.quascirev.2009.10.016>, 2010.
- 559 Faria, S. H., Weikusat, I., and Azuma, N.: The microstructure of polar ice. Part I: Highlights from ice core research, *J. Struct.  
560 Geol.*, 61, 2–20, <https://doi.org/10.1016/j.jsg.2013.09.010>, 2014.
- 561 Faria, S. H., Kipfstuhl, S., and Lambrecht, A.: The EPICA-DML Deep Ice Core: A Visual Record, Springer Berlin Heidelberg,  
562 Berlin, Heidelberg, 305 pp., <https://doi.org/10.1007/978-3-662-55308-4>, 2018.
- 563 Fegyveresi, J. M. and Alley, R. B.: South Pole Ice Core (SPIcecore) Visual Observations [data set],  
564 <https://doi.org/10.15784/601088>, 2018.
- 565 Fitzpatrick, J. J., Voigt, D. E., Fegyveresi, J. M., Stevens, N. T., Spencer, M. K., Cole-Dai, J., Alley, R. B., Jardine, G. E.,  
566 Cravens, E. D., Wilen, L. A., Fudge, T. J., and McConnell, J. R.: Physical properties of the WAIS Divide ice core, *J. Glaciol.*,  
567 60, 1181–1198, <https://doi.org/10.3189/2014JoG14J100>, 2014.
- 568 Fudge, T. J., Taylor, K. C., Waddington, E. D., Fitzpatrick, J. J., and Conway, H.: Electrical stratigraphy of the WAIS Divide  
569 ice core: identification of centimeter-scale irregular layering, *J. Geophys. Res. Earth Surf.*, 121, 1218–1229,  
570 <https://doi.org/10.1002/2016JF003845>, 2016.
- 571 Fudge, T. J., Hills, B. H., Horlings, A. N., Holschuh, N., Christian, J. E., Davidge, L., Hoffman, A., O’Connor, G. K.,  
572 Christianson, K., and Steig, E. J.: A site for deep ice coring at West Hercules Dome: results from ground-based geophysics  
573 and modeling, *J. Glaciol.*, 69, 538–550, <https://doi.org/10.1017/jog.2022.80>, 2023.
- 574 Fujita, S., Maeno, H., Uratsuka, S., Furukawa, T., Mae, S., Fujii, Y., and Watanabe, O.: Nature of radio echo layering in the  
575 Antarctic Ice Sheet detected by a two-frequency experiment, *J. Geophys. Res.*, 104, 13013–13024,  
576 <https://doi.org/10.1029/1999JB900034>, 1999.



- 577 Gow, A. J. and Meese, D.: Physical properties, crystalline textures and c-axis fabrics of the Siple Dome (Antarctica) ice core,  
578 *J. Glaciol.*, 53, 573–584, <https://doi.org/10.3189/002214307784409252>, 2007.
- 579 Gow, A. J., Epstein, S., and Sheehy, W.: On the origin of stratified debris in ice cores from the bottom of the Antarctic Ice  
580 Sheet, *J. Glaciol.*, 23, 185–192, <https://doi.org/10.3189/S0022143000029828>, 1979.
- 581 Gow, A. J., Meese, D. A., Alley, R. B., Fitzpatrick, J. J., Anandakrishnan, S., Woods, G. A., and Elder, B. C.: Physical and  
582 structural properties of the Greenland Ice Sheet Project 2 ice core: a review, *J. Geophys. Res.*, 102, 26559–26575,  
583 <https://doi.org/10.1029/97JC00165>, 1997.
- 584 Grootes, P. M., Steig, E. J., Stuiver, M., Waddington, E. D., Morse, D. L., and Nadeau, M.-J.: The Taylor Dome Antarctic  $^{18}\text{O}$   
585 record and globally synchronous changes in climate, *Quat. Res.*, 56, 289–298, <https://doi.org/10.1006/qres.2001.2276>, 2001.
- 586 Hamran, S., Aarholt, E., Hagen, J. O., and Mo, P.: Estimation of relative water content in a sub-polar glacier using surface-  
587 penetration radar, *J. Glaciol.*, 42, 533–537, 1996.
- 588 Jansen, D., Llorens, M.-G., Westhoff, J., Steinbach, F., Kipfstuhl, S., Bons, P., Griera, A., and Weikusat, I.: Small-scale  
589 disturbances in the stratigraphy of the NEEM ice core: observations and numerical model simulations, *The Cryosphere*  
590 *Discussions*, 9, <https://doi.org/10.5194/tcd-9-5817-2015>, 2015.
- 591 Johnsen, S. J., Clausen, H. B., Dansgaard, W., Gundestrup, N. S., Hammer, C. U., and Tauber, H.: The Eem stable isotope  
592 record along the GRIP ice core and its interpretation, *Quat. Res.*, 43, 117–124, <https://doi.org/10.1006/qres.1995.1013>, 1995.
- 593 Johnsen, S. J., Dahl-Jensen, D., Gundestrup, N., Steffensen, J. P., Clausen, H. B., Miller, H., Masson-Delmotte, V.,  
594 Sveinbjörnsdóttir, A. E., and White, J.: Oxygen isotope and palaeotemperature records from six Greenland ice-core stations:  
595 Camp Century, Dye-3, GRIP, GISP2, Renland and NorthGRIP, *J. Quat. Sci.*, 16, 299–307, <https://doi.org/10.1002/jqs.622>,  
596 2001.
- 597 Jouzel, J. and Masson-Delmotte, V.: Deep ice cores: the need for going back in time, *Quat. Sci. Rev.*, 29, 3683–3689,  
598 <https://doi.org/10.1016/j.quascirev.2010.10.002>, 2010.
- 599 Jouzel, J., Petit, J. R., Souchez, R., Barkov, N. I., Lipenkov, V. Ya., Raynaud, D., Stievenard, M., Vassiliev, N. I., Verbeke,  
600 V., and Vimeux, F.: More than 200 meters of lake ice above subglacial Lake Vostok, Antarctica, *Science*, 286, 2138–2141,  
601 <https://doi.org/10.1126/science.286.5447.2138>, 1999.
- 602 Jouzel, J., Masson-Delmotte, V., Cattani, O., Dreyfus, G., Falourd, S., Hoffmann, G., Minster, B., Nouet, J., Barnola, J. M.,  
603 Chappellaz, J., Fischer, H., Gallet, J. C., Johnsen, S., Leuenberger, M., Loulergue, L., Luethi, D., Oerter, H., Parrenin, F.,  
604 Raisbeck, G., Raynaud, D., Schilt, A., Schwander, J., Selmo, E., Souchez, R., Spahni, R., Stauffer, B., Steffensen, J. P., Stenni,  
605 B., Stocker, T. F., Tison, J. L., Werner, M., and Wolff, E. W.: Orbital and millennial Antarctic climate variability over the past  
606 800,000 years, *Science*, 317, 793–796, <https://doi.org/10.1126/science.1141038>, 2007.
- 607 Karlsson, N. B., Razik, S., Hörhold, M., Winter, A., Steinhage, D., Binder, T., and Eisen, O.: Surface accumulation in Northern  
608 Central Greenland during the last 300 years, *Ann. Glaciol.*, 61, 214–224, <https://doi.org/10.1017/aog.2020.30>, 2020.
- 609 Kipfstuhl, S.: Visual Stratigraphy of the NEEM Ice Core with Linescanner [data set],  
610 <https://doi.org/10.1594/PANGAEA.743062>, 2009.
- 611 Kluskiewicz, D., Waddington, E. D., Anandakrishnan, S., Voigt, D. E., Matsuoka, K., and McCarthy, M. P.: Sonic methods  
612 for measuring crystal orientation fabric in ice, and results from the West Antarctic Ice Sheet (WAIS) Divide, *J. Glaciol.*, 63,  
613 603–617, <https://doi.org/10.1017/jog.2017.20>, 2017.





- 614 Landais, A., Chappellaz, J., Delmotte, M., Jouzel, J., Blunier, T., Bourq, C., Caillon, N., Cherrier, S., Malaizé, B., Masson-  
615 Delmotte, V., Raynaud, D., Schwander, J., and Steffensen, J. P.: A tentative reconstruction of the last interglacial and glacial  
616 inception in Greenland based on new gas measurements in the Greenland Ice Core Project (GRIP) ice core, *J. Geophys. Res.*  
617 *Atm.*, 108, <https://doi.org/10.1029/2002JD003147>, 2003.
- 618 Langway, C. C., Shoji, H., and Azuma, N.: Crystal size and orientation patterns in the Wisconsin-age ice from Dye 3,  
619 Greenland, *Ann. Glaciol.*, 10, 109–115, <https://doi.org/10.3189/S0260305500004262>, 1988.
- 620 Leysinger Vieli, G. J.-M. C., Hindmarsh, R. C. a, and Siegert, M. J.: Three-dimensional flow influences on radar layer  
621 stratigraphy, *Ann. Glaciol.*, 22–28, 2007.
- 622 Lilien, D. A., Steinhage, D., Taylor, D., Parrenin, F., Ritz, C., Mulvaney, R., Martín, C., Yan, J.-B., O’Neill, C., Frezzotti, M.,  
623 Miller, H., Gogineni, P., Dahl-Jensen, D., and Eisen, O.: Brief communication: new radar constraints support presence of ice  
624 older than 1.5 Myr at Little Dome C, *The Cryosphere*, 15, 1881–1888, <https://doi.org/10.5194/tc-15-1881-2021>, 2021.
- 625 Lipenkov, V. Ya. and Raynaud, D.: The Mid-Pleistocene transition and the Vostok oldest ice challenge, *Ice and Snow*, 55, 95–  
626 106, <https://doi.org/10.15356/2076-6734-2015-4-95-106>, 2015.
- 627 Miyamoto, A., Weikusat, I., and Hondoh, T.: Complete determination of ice crystal orientation using Laue X-ray diffraction  
628 method, *J. Glaciol.*, 57, 103–110, <https://doi.org/10.3189/002214311795306754>, 2011.
- 629 Mojtabavi, S., Eisen, O., Franke, S., Jansen, D., Steinhage, D., Paden, J., Dahl-Jensen, D., Weikusat, I., Eichler, J., and  
630 Wilhelms, F.: Origin of englacial stratigraphy at three deep ice core sites of the Greenland Ice Sheet by synthetic radar  
631 modelling, *J. Glaciol.*, 68, 799–811, <https://doi.org/10.1017/jog.2021.137>, 2022.
- 632 Montagnat, M., Buiron, D., Arnaud, L., Broquet, A., Schlitz, P., Jacob, R., and Kipfstuhl, S.: Measurements and numerical  
633 simulation of fabric evolution along the Talos Dome ice core, Antarctica, *Earth and Planetary Science Letters*, 357–358, 168–  
634 178, <https://doi.org/10.1016/j.epsl.2012.09.025>, 2012.
- 635 Montagnat, M., Azuma, N., Dahl-Jensen, D., Eichler, J., Fujita, S., Gillet-Chaulet, F., Kipfstuhl, S., Samyn, D., Svensson, A.,  
636 and Weikusat, I.: Fabric along the NEEM ice core, Greenland, and its comparison with GRIP and NGRIP ice cores, *The*  
637 *Cryosphere*, 8, 1129–1138, <https://doi.org/10.5194/tc-8-1129-2014>, 2014.
- 638 Mulvaney, R., Rix, J., Polfrey, S., Grieman, M., Martin, C., Nehrbass-Ahles, C., Rowell, I., Tuckwell, R., and Wolff, E.: Ice  
639 drilling on Skytrain Ice Rise and Sherman Island, Antarctica, *Ann. Glaciol.*, 62, 311–323, <https://doi.org/10.1017/aog.2021.7>,  
640 2021.
- 641 NEEM Community Members: Eemian interglacial reconstructed from a Greenland folded ice core, *Nature*, 493, 489–494,  
642 <https://doi.org/10.1038/nature11789>, 2013.
- 643 North Greenland Ice Core Project Members: High-resolution record of Northern Hemisphere climate extending into the last  
644 interglacial period, *Nature*, 431, 147–151, <https://doi.org/10.1038/nature02805>, 2004.
- 645 Obbard, R. and Baker, I.: The microstructure of meteoric ice from Vostok, Antarctica, *J. Glaciol.*, 53, 41–62,  
646 <https://doi.org/10.3189/172756507781833901>, 2007.
- 647 Petit, J. R., Jouzel, J., Raynaud, D., Barkov, N. I., Delaygue, G., Delmotte, M., Kotlyakov, V. M., Legrand, M., Lipenkov, V.  
648 Y., Lorius, C., and Saltzman, E.: Climate and atmospheric history of the past 420,000 years from the Vostok ice core,  
649 Antarctica, *Nature*, 399, 1999.



- 650 Raynaud, D., Barnola, J.-M., Souchez, R., Lorrain, R., Petit, J.-R., Duval, P., and Lipenkov, V. Y.: The record for marine  
651 isotopic stage 11, *Nature*, 436, 39–40, <https://doi.org/10.1038/43639b>, 2005.
- 652 Ruth, U., Kaufmann, P., Kipfstuhl, S., Lambrecht, A., Morganti, A., Oerter, H., Parrenin, F., Rybak, O., Severi, M., Udisti, R.,  
653 Wilhelms, F., and Wolff, E.: “EDML1”: a chronology for the EPICA deep ice core from Dronning Maud Land, Antarctica,  
654 over the last 150 000 years, *Clim. Past*, 2007.
- 655 Saruya, T., Fujita, S., Iizuka, Y., Miyamoto, A., Ohno, H., Hori, A., Shigeyama, W., Hirabayashi, M., and Goto-Azuma, K.:  
656 Development of crystal orientation fabric in the Dome Fuji ice core in East Antarctica: implications for the deformation regime  
657 in ice sheets, *The Cryosphere*, 16, 2985–3003, <https://doi.org/10.5194/tc-16-2985-2022>, 2022.
- 658 Saruya, T., Miyamoto, A., Fujita, S., Goto-Azuma, K., Hirabayashi, M., Hori, A., Igarashi, M., Iizuka, Y., Kameda, T., Ohno,  
659 H., Shigeyama, W., and Tsutaki, S.: Development of deformational regimes and microstructures in the deep sections and  
660 overall layered structures of the Dome Fuji ice core, Antarctica, *EGUsphere*, 1–48, <https://doi.org/10.5194/egusphere-2023-3146>, 2024.
- 662 Schroeder, D. M., Blankenship, D. D., Raney, R. K., and Grima, C.: Estimating subglacial water geometry using radar bed  
663 echo specularity: application to Thwaites Glacier, West Antarctica, *IEEE Geosci. Remote Sensing Lett.*, 12, 443–447,  
664 <https://doi.org/10.1109/LGRS.2014.2337878>, 2015.
- 665 Schroeder, D. M., Bingham, R. G., Blankenship, D. D., Christianson, K., Eisen, O., Flowers, G. E., Karlsson, N. B., Koutnik,  
666 M. R., Paden, J. D., and Siegert, M. J.: Five decades of radioglaciology, *Ann. Glaciol.*, 61, 1–13,  
667 <https://doi.org/10.1017/aog.2020.11>, 2020.
- 668 Souchez, R., Petit, J. R., Jouzel, J., Simões, J., De Angelis, M., Barkov, N., Stievenard, M., Vimeux, F., Sleewaegen, J., and  
669 Lorrain, R.: Highly deformed basal ice in the Vostok core, Antarctica, *Geophys. Res. Lett.*, 29,  
670 <https://doi.org/10.1029/2001GL014192>, 2002.
- 671 Steig, E. J., Brook, E. J., White, J. W. C., Sucher, C. M., Bender, M. L., Lehman, S. J., Morse, D. L., Waddington, E. D., and  
672 Clow, G. D.: Synchronous climate changes in Antarctica and the North Atlantic, *Science*, 282, 92–95,  
673 <https://doi.org/10.1126/science.282.5386.92>, 1998.
- 674 Stillman, D. E., MacGregor, J. a., and Grimm, R. E.: The role of acids in electrical conduction through ice, *J. Geophys. Res.*  
675 *Earth Surf.*, 118, 1–16, <https://doi.org/10.1029/2012JF002603>, 2013.
- 676 Svensson, A.: Visual stratigraphy of the North Greenland Ice Core Project (NorthGRIP) ice core during the last glacial period,  
677 *J. Geophys. Res.*, 110, <https://doi.org/10.1029/2004JD005134>, 2005.
- 678 Takata, M., Iizuka, Y., Hondoh, T., Fujita, S., Fujii, Y., and Shoji, H.: Stratigraphic analysis of Dome Fuji Antarctic ice core  
679 using an optical scanner, *Ann. Glaciol.*, 39, 467–472, <https://doi.org/10.3189/172756404781813899>, 2004.
- 680 Thorsteinsson, T., Kipfstuhl, J., and Miller, H.: Textures and fabrics in the GRIP ice core, *J. Geophys. Res. Oceans*, 102,  
681 26583–26599, <https://doi.org/10.1029/97JC00161>, 1997.
- 682 Tison, J.-L., de Angelis, M., Littot, G., Wolff, E., Fischer, H., Hansson, M., Bigler, M., Udisti, R., Wegner, A., Jouzel, J.,  
683 Stenni, B., Johnsen, S., Masson-Delmotte, V., Landais, A., Lipenkov, V., Loulergue, L., Barnola, J.-M., Petit, J.-R., Delmonte,  
684 B., Dreyfus, G., Dahl-Jensen, D., Durand, G., Bereiter, B., Schilt, A., Spahni, R., Pol, K., Lorrain, R., Souchez, R., and Samyn,  
685 D.: Retrieving the paleoclimatic signal from the deeper part of the EPICA Dome C ice core, *The Cryosphere*, 9, 1633–1648,  
686 <https://doi.org/10.5194/tc-9-1633-2015>, 2015.



- 687 Turkeev, A. V., Vasilev, N. I., Lipenkov, V. Y., Bolshunov, A. V., Ekaykin, A. A., Dmitriev, A. N., and Vasilev, D. A.:  
688 Drilling the new 5G-5 branch hole at Vostok Station for collecting a replicate core of old meteoric ice, *Ann. Glaciol.*, 62, 305–  
689 310, <https://doi.org/10.1017/aog.2021.4>, 2021.
- 690 Verbeke, V., Lorrain, R., Johnsen, S. J., and Tison, J.-L.: A multiple-step deformation history of basal ice from the Dye 3  
691 (Greenland) core: new insights from the CO<sub>2</sub> and CH<sub>4</sub> content, *Ann. Glaciol.*, 35, 231–236,  
692 <https://doi.org/10.3189/172756402781817248>, 2002.
- 693 Wang, Y., Thorsteinsson, T., Kipfstuhl, J., Miller, H., Dahl-Jensen, D., and Shoji, H.: A vertical girdle fabric in the NorthGRIP  
694 deep ice core, North Greenland, *Ann. Glaciol.*, 35, 515–520, <https://doi.org/10.3189/172756402781817301>, 2002.
- 695 Wang, Z., Chung, A., Steinhage, D., Parrenin, F., Freitag, J., and Eisen, O.: Mapping age and basal conditions of ice in the  
696 Dome Fuji region, Antarctica, by combining radar internal layer stratigraphy and flow modeling, *The Cryosphere*, 17, 4297–  
697 4314, <https://doi.org/10.5194/tc-17-4297-2023>, 2023.
- 698 Weikusat, I., Kipfstuhl, S., and Lambrecht, A.: Crystal c-axes (Fabric G20) of Ice Core Samples Collected from the EDML  
699 Ice Core with Links to Raw Data Files [data set], <https://doi.org/10.1594/PANGAEA.807207>, 2013.
- 700 Weikusat, I., Jansen, D., Binder, T., Eichler, J., Faria, S. H., Wilhelms, F., Kipfstuhl, S., Sheldon, S., Miller, H., Dahl-Jensen,  
701 D., and Kleiner, T.: Physical analysis of an Antarctic ice core—towards an integration of micro- and macrodynamics of polar  
702 ice, *Phil. Trans. R. Soc. Lond. A*, 375, 20150347, <https://doi.org/10.1098/rsta.2015.0347>, 2017.
- 703 Wilson, C. J. L., Russell-Head, D. S., and Sim, H. M.: The application of an automated fabric analyzer system to the textural  
704 evolution of folded ice layers in shear zones, *Ann. Glaciol.*, 37, 7–17, <https://doi.org/10.3189/172756403781815401>, 2003.
- 705 Winter, A., Steinhage, D., Arnold, E. J., Blankenship, D. D., Cavitte, M. G. P., Corr, H. F. J., Paden, J. D., Urbini, S., Young,  
706 D. A., and Eisen, O.: Comparison of measurements from different radio-echo sounding systems and synchronization with the  
707 ice core at Dome C, Antarctica, *The Cryosphere*, 11, 653–668, <https://doi.org/10.5194/tc-11-653-2017>, 2017.
- 708 Winter, K., Woodward, J., Ross, N., Dunning, S. A., Hein, A. S., Westoby, M. J., Culberg, R., Marrero, S. M., Schroeder, D.  
709 M., Sugden, D. E., and Siegert, M. J.: Radar-detected englacial debris in the West Antarctic Ice Sheet, *Geophys. Res. Lett.*,  
710 46, 10454–10462, <https://doi.org/10.1029/2019GL084012>, 2019.
- 711 Wolff, E. W.: Electrical stratigraphy of polar ice cores: principles, methods, and findings, in: *Physics of Ice Core Records*,  
712 *International Symposium on Physics of Ice Core Records*. Shikotsukohan, Hokkaido, Japan, 155–171, 2000.
- 713 Wolff, E. W., Barbante, C., Becagli, S., Bigler, M., Boutron, C. F., Castellano, E., De Angelis, M., Federer, U., Fischer, H.,  
714 Fundel, F., Hansson, M., Hutterli, M., Jonsell, U., Karlin, T., Kaufmann, P., Lambert, F., Littot, G. C., Mulvaney, R.,  
715 Röthlisberger, R., Ruth, U., Severi, M., Siggaard-Andersen, M. L., Sime, L. C., Steffensen, J. P., Stocker, T. F., Traversi, R.,  
716 Twarloh, B., Udisti, R., Wagenbach, D., and Wegner, A.: Changes in environment over the last 800,000 years from chemical  
717 analysis of the EPICA Dome C ice core, *Quat. Sci. Rev.*, 29, 285–295, <https://doi.org/10.1016/j.quascirev.2009.06.013>, 2010.